Advanced Ceramics Progress

Research Article

Journal Homepage: www.acerp.ir

Nanostructuring Platinum nanoparticles on $Ni/Ce_{0.8}Gd_{0.2}O_{2-\delta}$ anode for low-temperature solid oxide fuel cell via single-step infiltration: a case study

F. S. Torknik*[a], G. M. Choi[b], A. Maghsoudipour[a], M. Keyanpour-Rad[a]

[a]*Department of Ceramic, Materials and Energy Research Center, Karaj, Iran*
[b]*Fuel C ell Research Center and Department of Materials Science and Engineering, Pohang University of Science and Technology, Pohang, Korea*

PAPER INFO

Paper history:
Received 02 September 2018
Accepted in revised form 10 October 2018

Keywords:
LTSOFC
Ni/GDC20 Anode
Platinum Infiltration
Pt-Nanoparticles
$H_2PtCl_6.6H_2O$

ABSTRACT

With the aim of promoting the $Ni/Ce_{0.8}Gd_{0.2}O_{2-\delta}$ (Ni/GDC20) cermet anodic performance of low-temperature solid oxide fuel cell (LT-SOFC), nanostructuring platinum nanoparticles on NiO/GDC composite was executed by single-step wet-infiltration of hexachloroplatinic acid hexahydrate ($H_2PtCl_6.6H_2O$) precursor on the NiO/GDC20 composite. The anodic polarization resistance was measured using symmetric Ni–GDC20|GDC20|Pt electrolyte-supported cell at a temperature range of 400 to 600 °C. Microstructural refinement was studied by field emission scanning electron microscopy (FE-SEM) and transmission electron microscopy (TEM) techniques in comparison to the bare anode before and after hydrogen reduction at 600 °C and also after anodic performance test. Nanostructuring Pt-nanoparticles with an average particle size of 12.5 nm on Ni/GDC20 anode indicated the lack of electrocatalytic enhancement with the addition of platinum for H_2 oxidation reaction in LT-SOFC.

1. INTRODUCTION

The low-temperature solid oxide fuel cell (LT-SOFC) anodes with active triple phase boundaries (TPBs) have an important role on the performance, durability and energy conversion process of LT-SOFC due to the electro-oxidation reaction of the fuel at the anode at 400-600 ˚C [1-3] . Nanostructuring by infiltration method owing to much less necessary material, lower processing temperature, smaller particle size, unique morphology of coating and higher TPB density has been led to the higher performance of infiltrated anodes than conventional ones [4]. For Ni-cermets such as Nickel/gadolinia-doped ceria (Ni/GDC) and Ni/Samaria-doped ceria (Ni/SDC) having good LT-SOFC performance [5], only a few researchers have investigated on the infiltration using metals (like palladium, rhodium and molybdenum) [6-8] and mixed ionic and electronic conductors (MIEC) (namely SDC, GDC, and $BaCe_{0.9}Yb_{0.1}O_{3-\delta}$ (BCYb)) [9-11].

One of the most valuable metal electrocatalysts is platinum, which is commonly used for electrodes of LT-SOFC due to high selectivity, activity, stability, and electronic conductivity for the H_2 oxidation reaction (HOR) at the anode or the O_2 reduction reaction (ORR) at the cathode [12-14]. Certainly, Pt loading for the HOR because of its quick performance is much lower than the ORR one [14]. Study of the nanostructured porous Pt catalyst layer deposition (as atomic laser deposition Pt (cathode)|YSZ (electrolyte)|atomic laser deposition Pt|sputtered Pt (anode)) for LT-SOFC shows the improvement of electrochemical performance. In this type of catalyst, there are a high TPB density and a 90% fuel cell's peak power density at 400 °C relative to the original fuel cell (atomic laser deposition Pt (cathode)|YSZ (electrolyte)|sputtered Pt (anode)) [15]. An ultra-thin Pt functional layer between the Ni/GDC anode and GDC electrolyte for the H_2 oxidation reaction indicates twice-higher catalytic activity than Ni and much higher electronic conductivity than Ni-GDC cermet [16]. The performance of binary and ternary electrocatalyst infiltrated $Sr_{0.94}Ti_{0.9}Nb_{0.1}O_3$ (STN) anodes for LT-SOFC shows that Pt as Pt-GDC as well as Ni-Pt-GDC exhibits the lowest polarization resistance on the STN anode [17]. Moreover, Pt-GDC impregnated $La_{0.20}Sr_{0.25}Ca_{0.45}TiO_3$ (LSCT) anodes display very promising performance during short-term electrochemical testing in humidified hydrogen for LT-SOFC [18].

According to the literature, it seems that further investigations are clearly required to evaluate the influence of platinum nanoparticles on the microstructure and electrochemical performance of the

*Corresponding Author's Email: fstorknik@gmail.com (F.Torknik)

Ni/GDC anode. Hence, in this work, based on the world price and necessity of cost-effective application of precious metals, the infiltration of platinum precursor solution is considered just once in order to fabricate Pt-Ni/$Ce_{0.8}Gd_{0.2}O_{2-\delta}$.

2. EXPERIMENTAL PROCEDURES

In this research, the configuration of planar electrolyte-supported Ni–GDC20|GDC20 half-cell was used [1]. Dense GDC20 electrolyte discs in a diameter of 15 mm and thickness of 0.3–0.4 mm were prepared. A homogenized paste of the modified $NiO_{0.6}$/$GDC20_{0.4}$ powder and the organic screen-printing solution was applied on the center of the electrolyte in a circular shape, which was followed through firing at 1350 °C for 2 h to attain a porous composite with ~15 μm thickness and 0.5 cm^2 in area.

In order to make Pt-infiltrated Ni/GDC20 anode, the platinum containing solution (0.1 mol/L) was prepared via dissolving hexachloroplatinic acid hexahydrate ($H_2PtCl_6.6H_2O$, MERCK) precursor in some deionized water. Infiltration was performed using a microsyringe via placing only a droplet of the solution on the porous NiO/GDC20 structure as an original composite. The excess solution was eliminated from the surface of the anode and followed by calcination at 600 °C in the air for 1h. The anodic impedance of the Pt-infiltrated Ni/GDC20 anode was tested using a three-electrode array in a two-chamber conditions comparing to the original one (Ni/GDC20).

Pt paste was painted as the counter and reference electrodes, symmetrically opposite to the working electrode and a small point at the electrolyte edge with 3 mm-distance from the counter electrode, respectively. In addition, Pt mesh was used as a current-collector in an intimate contact with the electrodes. Before testing, NiO was reduced in-situ at 600 °C in the H_2 for 1h. The impedance spectra of the anode were collected under open circuit voltage at the temperature range of 400–600 °C. Humidified hydrogen (3 vol.% H_2O) was utilized as the fuel gas with a flow rate of 80 cc/min and open air as the oxidant. Morphological inspection of the fabricated composites/cermets/anodes was accomplished using field emission scanning electron microscopy (FE-SEM) in secondary electron (SE) mode without any coating materials. Detailed microstructure of the aforementioned specimens was studied by high-resolution transmission electron microscopy (HR-TEM) in bright field (BF) and dark field (DF) modes. TEM specimen preparation was carried out by suspension evaporation on the ultra-thin holey carbon support having 300 mesh copper grid. The average particle size of the specimens was determined using Digital Micrograph ™ from 100 nanoparticles as a minimum in an arbitrarily selected area [6].

3. RESULTS AND DISCUSSION

3.1. Microstructure

Fig. 1(A-E) shows SE-SEM microphotographs of the original NiO/GDC20 (denoted with O– prefix) and Pt-infiltrated NiO/GDC20 (denoted with T– prefix) composites before and after H_2 reduction (denoted with –O suffix as an oxide composite and with –R suffix as a reduced cermet, respectively) as well as after anode testing (denoted with –AT suffix). The microstructure of O-O composite (pure NiO/GDC20 before H_2 reduction in Fig. 1(A)) reveals the particle size of 0.3 μm and a porosity of 34%. It should be also mentioned that NiO and GDC20 have a grain size of 132 nm and 145 nm, respectively. Fig. 1(D) exhibits a micrograph of T-O composite (Pt-infiltrated NiO/GDC20 before H_2 reduction) indicating the copious distribution of nanoparticle lumps in a disordered shape on the cermet surface. Fig. 2(A) also shows a typical high-resolution SEM image of T-O composite accompanied with typical insets of A, B, C, and D denoting line-profile inspection of coverage on the composite surface of T-O. The absence of particles with clean surfaces in the T-O composite and the fairly uniform distribution of the infiltrated nanoparticles together with their aggregation on the cermet surface (Figs. 1(D) and 2(A)) compared to O-O composite (Fig. 1(A)) is related to a full coverage of the NiO/GDC20 surface only with a slight loading of ~ 0.03 mg/cm^2. In this light, characterization of the magnified image of Fig. 2(A) demonstrates a nano-grained network with an average nanoparticle size of 14.7 nm on the T-O composite. In explanation of this matter, it should be stated that the decomposition of $H_2PtCl_6.6H_2O$ below the calcination temperature of 600 °C together with the most probable appearance of PtO or PtO_2 [19] with melting point of 550 °C or 450 °C, respectively (Table 1), can be led to the coalescence and sintering of the oxide nanoparticles (Figs. 1(D) and 2(A)).

TABLE 1. The Values of melting, Hüttig, and Tamman temperatures for platinum compounds [20]

Compound	$T_{melting}$ (°C)	$T_{Hüttig}$ (°C)	T_{Tamman} (°C)
Pt	1,755	335	841
PtO	550	-26	139
PtO_2	450	-56	89
$PtCl_2$	581	-17	154
$PtCl_4$	370	-80	49

The reduction of NiO to Ni leads to 41 vol% shrinkage and 43% porosity. Moreover, a fine-grained cermet (O-R in Fig. 1(B)) were obtained containing Ni and GDC20 with grain sizes of 30 nm and 207 nm, respectively [6]. Fig. 1(E) shows SE-SEM micrograph of T-R cermet

(Pt-infiltrated NiO/GDC20 after H_2 reduction) representing nanoparticle aggregates on the cermet surface. In addition, Fig. 2(B) shows a typical high-resolution SEM image of T-R cermet accompanied with the insets of E, F, G, and H, which are indicated the line-profile of coverage on the cermet surface with an average nanoparticle size of 12.3 nm. Hydrogen reduction of the T-O composite due to the fast and complete reduction of Pt-oxide(s) to metallic Pt (Pt^0) [21] was principally led to the volume deoxidizing shrinkage of 39% of PtO and 59% of PtO_2 to Pt^0 (see Table 2), nanoporosity in the nanoparticle network and spheroidizing of Pt^0-nanoparticle aggregates on the cermet surface (Fig. 2(B)).

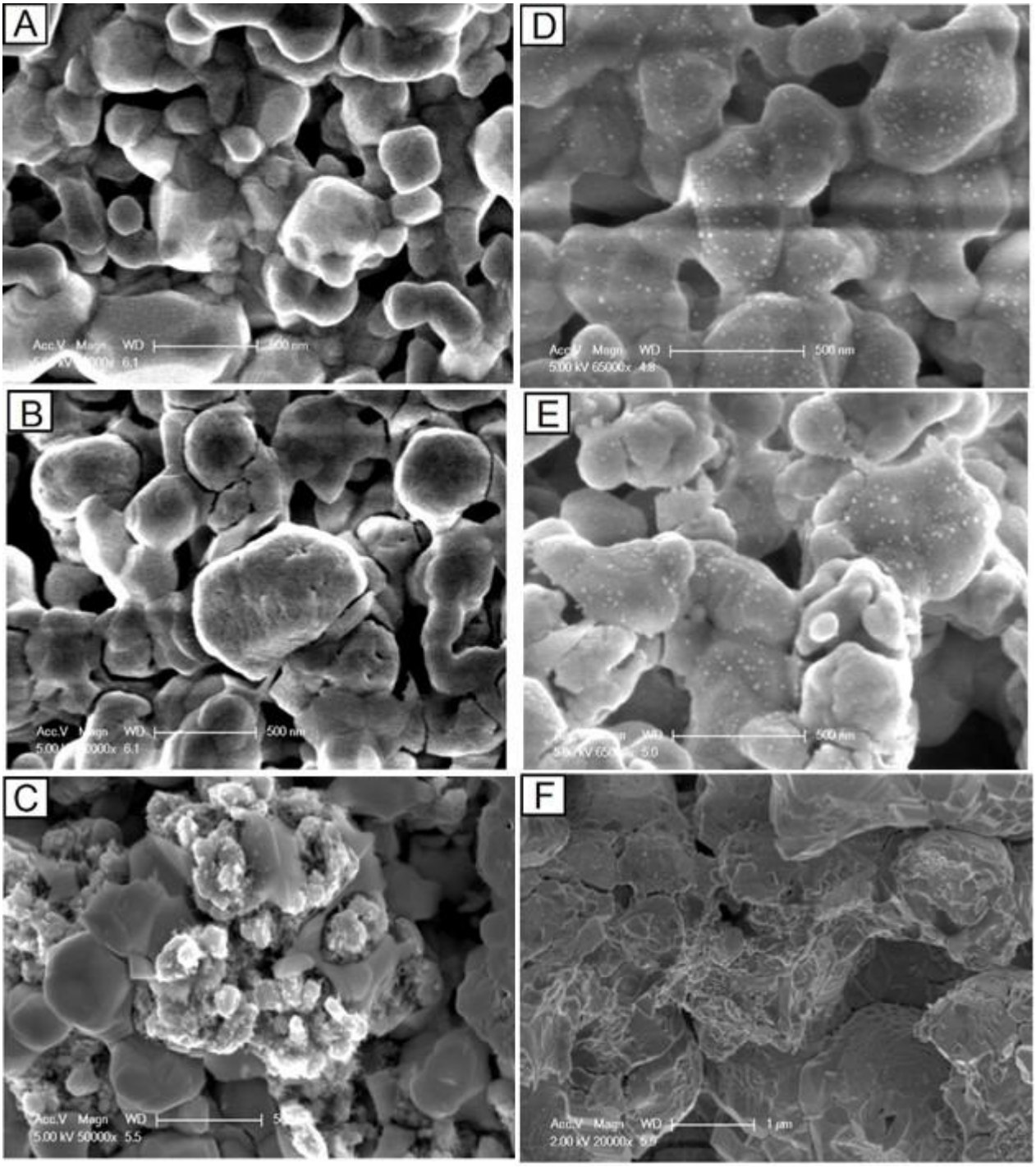

Figure 1. SEM microphotographs of NiO/GDC20 composites with/without infiltration of Pt-nanoparticles before and after hydrogen reduction and also after impedance test: (A) O-O, (B) O-R, and (C) O-AT [6], (D) T-O, (E) T-R, and (F) T-AT

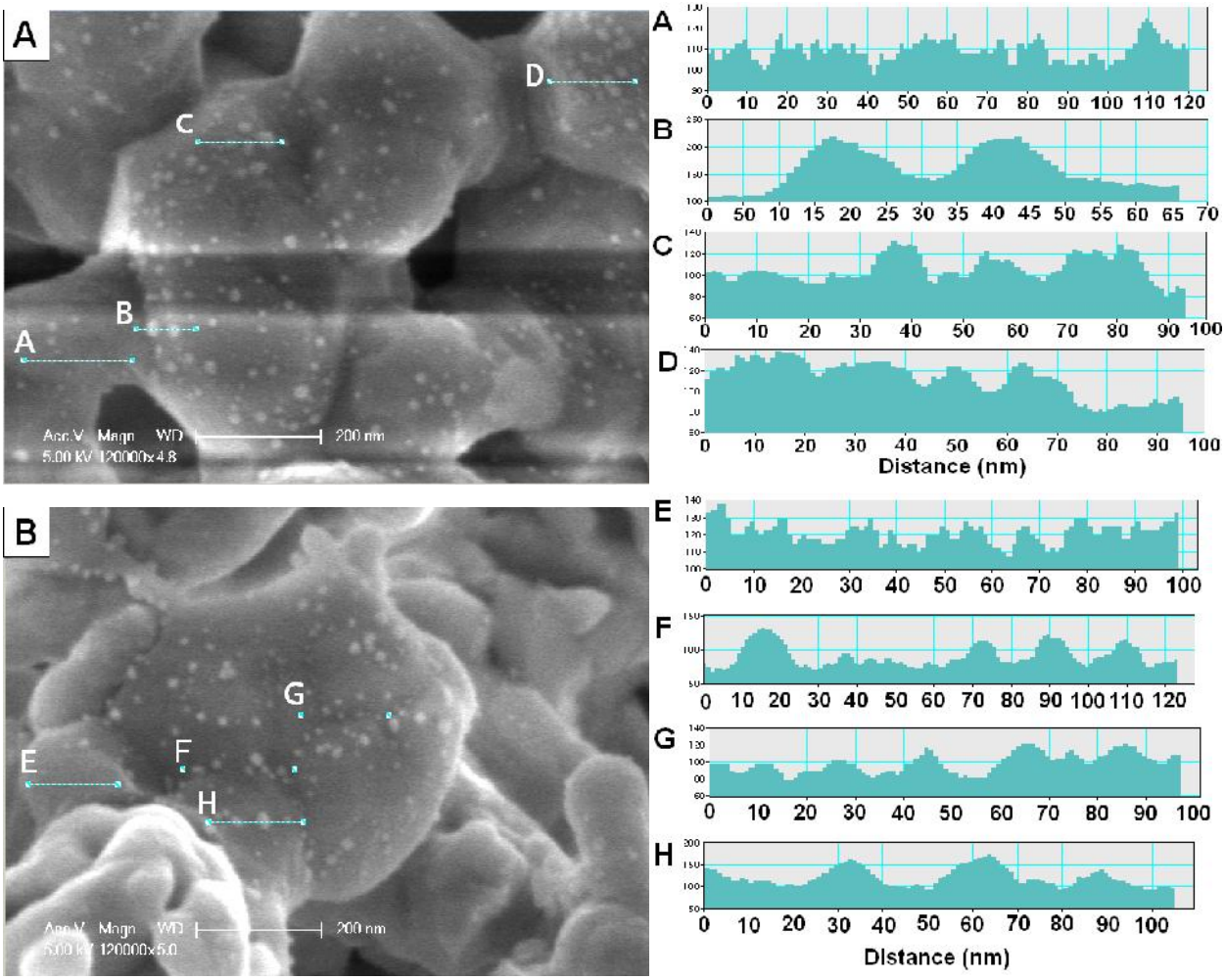

Figure 2. The high-resolution SEM microphoto raphs of Pt-NiO/GDC20 composite (A) before H_2 reduction as T-O composite and (B) after H_2 reduction as T-R composite with the particles coverage line-profile

TABLE 2. The molar mass, specific mass and molar volume of PtO and Pt^0

	PtO	**PtO_2**	**Pt^0**
M (g/mol)	211.083	227.08 [22]	195.084 [23]
ρ (g/cm^3)	14.1	10.2	21.45 [24]
V (cm^3/mol)	14.97	22.26	9.09

Evaluating TEM micrographs related to the T-R composite (Fig. 3(A)) with knowledge of the anode particles identification [6] shows the isolated pseudo-spherical nanoparticles on the left-edge of Ni particle and the spreading of smaller nanoparticles without coarsening on the upper-edge of the GDC20 particles. Investigation of BF and DF-TEM images, as typically seen in Fig. 3(B), clearly reveals bright contrast of crystalline nanoparticles on the lower-edge of cermet particles than the matrix, which indicates the individual crystallographic phase of the infiltrated nanoparticles established upon the diffraction contrast.

The Pt-nanoparticles size histogram in the T-R composite (Fig. 3(C)) specifies the average nanoparticle size of ~ 12.5 nm that is compatible to the SEM results (12.3 nm). The low tendency of the Pt-infiltrated nanoparticles to severe sintering during the H_2 reduction contrary to Pt-oxide nanoparticles is initiated from less mobility of Pt-atoms in the sintering based on the Hüttig and Tamman temperatures of the metal platinum (Table 1) [20].

Additionally, the low partial pressure of Pt^0 catalyst during the cell testing in a hydrogen environment at a temperature range of 400-600 ˚C and a pressure range of 10^{-31}-10^{-21} Pa [25] is impeded Pt^0-volatility and decelerated thermal degradation of Pt^0-nanoparticles via sintering and subsequent coarsening in LT-SOFC (Fig. 1(F)). Consequently, it is expected that maintaining

smaller lumps of Pt^0-particles can be helpful in order to preserve the high activity of Pt^0-nanocatalysts in SOFC.

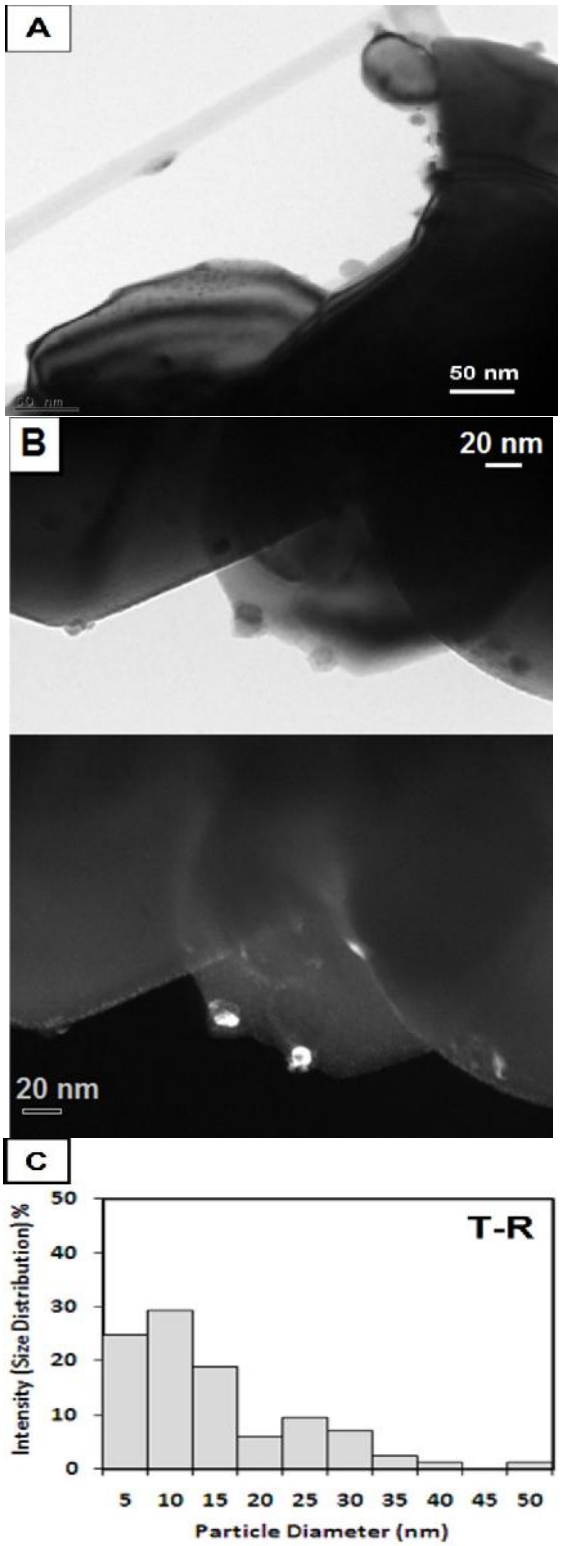

Figure 3. Typical TEM images (A) in a bright field mode, (B) in bright and dark field modes and (C) nanoparticle size histogram of T-R

3.2. Anode performance

Fig. 4 shows typical anodic impedance spectra for the H_2 oxidation reaction on the O-R [1] and T-R anodes in the temperature range of 400-600 °C with no arc separation in the studied impedance frequency range.

The anodic polarization resistance (R_a) data for the anodes at all the testing temperatures have been listed in Table 3, indicating too much increase of the R_a in Pt-infiltrated anode (≥ 36.5%) than that in the O-R one. The supreme catalytic ability of platinum in order to supply the high exchange-current densities in LT-SOFCs has been confirmed [26]. Nevertheless, the lack of coarsening propensity of Pt^0-nanoparticles in LT-SOFC conditions cannot be beneficial for its effective electrocatalytic activity on the Ni/GDC20 anode, so, it lowers anode polarization resistance of O-R. Therefore, besides the catalyst composition, its local abundance on the cermet microstructure can be also important. Based on the above-mentioned results, PT seems as an ineffectual infiltrated nanocatalyst in the current study.

TABLE 3. The values of anode polarization resistance for the H_2 oxidation reaction on the O-R and T-R anodes at the testing temperatures in 97% H_2/3% H_2O at open circuit

T (°C) / Sample	R_a ($\Omega.cm^2$)				
	600	550	500	450	400
O-R [1]	0.64	3.96	37.96	181.36	268.62
T-R	1.23	8.26	52.12	247.47	729.06

4. CONCLUSION

The investigation of nanostructuring Ni/GDC20 anode via Pt-infiltration with the only addition of one drop of $H_2PtCl_6.6H_2O$ precursor solution was conducted on the anodic polarization resistance for H_2 oxidation reaction at 400-600 °C in comparison to the base anode. Regardless of the less coarsening propensity of Pt-nanoparticles with an average size of ~ 12.5 nm as well as the negligible volatility of platinum based on thermodynamic data during the cell testing in a hydrogen environment at temperatures of LT-SOFC, the anodic performance of Pt-infiltrated anode was much worse (≥ 36%) than that in the base Ni/GDC20 anode. This indicated that platinum is an ineffectual infiltrated nanocatalyst in the current study.

5. ACKNOWLEDGMENTS

Financial support by the Pohang University Science and Technology (POSTECH) of Republic of Korea and Materials and Energy Research Center (MERC) of Iran are gratefully acknowledged.

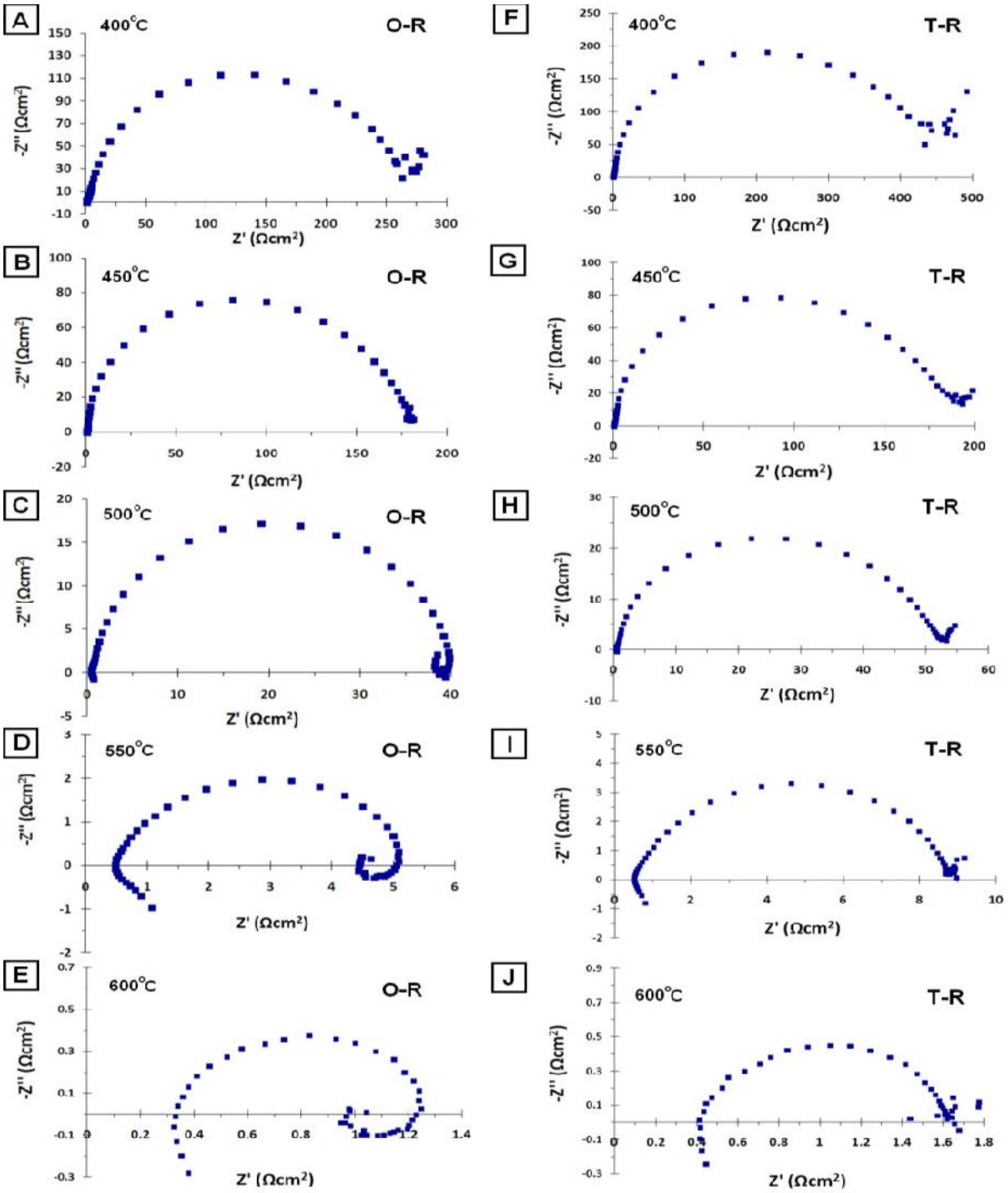

Figure 4. The anodic impedance spectra for the H_2 oxidation reaction on the O-R and T-R anodes as a function of temperature in 97% H_2/3% H_2O at the open circuit

REFERENCES

1. Torknik, F.S., Keyanpour-Rad, M., Maghsoudipour, A., Choi, G.M., "Effect of microstructure refinement on performance of $Ni/Ce_{0.8}Gd_{0.2}O_{1.9}$ anodes for low temperature solid oxide fuel cell", ***Ceramics International***, Vol. 40, No. 1, (2014), 1341-1350.
2. Chueh, W.C., Hao, Y., Jung, W., Haile, S.M., "High electrochemical activity of the oxide phase in model ceria–Pt and ceria–Ni composite anodes", ***Nature Materials***, Vol. 11, No. 2. (2012), 155-161.
3. Ni M., Zhao T.S. (Eds.), "Solid Oxide Fuel Cells: From Materials to System Modeling", Cambridge: Royal Society of Chemistry, (2013).
4. Reszka, A.J., Snyder, R.C., Gross, M. D., "Insights into the design of SOFC infiltrated electrodes with optimized active

TPB density via mechanistic modeling", ***Journal of The Electrochemical Society***, Vol. 161, No. 12, (2014), 1176-1183.

5. Gao, Z., Mogni, L.V., Miller, E.C., Railsback, J.G., Barnett, S.A., "A perspective on low-temperature solid oxide fuel cells", ***Energy & Environmental Science***, Vol. 9, No. 5, (2016), 1602-1644.
6. Torknik, F.S., Maghsoudipour, A., Keyanpour-Rad, M., Choi, G.M., Oh, S.H., Shin, G.Y., "Microstructural refinement of Ni/$Ce_{0.8}Gd_{0.2}O_{2-\delta}$ anodes for low-temperature solid oxide fuel cell by wet infiltration loading of $PdCl_2$", ***Ceramics International***, Vol. 40, No. 8, (2014), 12299-12312.
7. Torknik, F.S., Keyanpour-Rad, M., Maghsoudipour, A., Choi, G.M., "Effect of rhodium infiltration on the microstructure and performance of Ni/$Ce_{0.8}Gd_{0.2}O_{2-\delta}$ cermet anode for low temperature solid oxide fuel cell", ***Iranian Journal of Materials Science and Engineering***, Vol. 13, No. 1, (2016), 43-49.
8. Li, P., Yu, B., Li, J., Yao, X., Zhao, Y., Li, Y., "Improved activity and stability of Ni-$Ce_{0.8}Sm_{0.2}O_{1.9}$ anode for solid oxide fuel cells fed with methanol through addition of molybdenum", ***Journal of Power Sources***, Vol. 320, (2016), 251-256.
9. Liu, Z., Ding, D., Liu, B., Guo, W., Wang, W., Xia, C., "Effect of impregnation phases on the performance of Ni-based anodes for low temperature solid oxide fuel cells", ***Journal of Power Sources***, Vol. 196, No. 20, (2011), 8561-8567.
10. Yoon, H.S., Gore, C.M., Lidie, A.A., Lee, K.T., Wachsman, E. D., "Process Integration for Scale-Up of $Ce_{0.9}Gd_{0.1}O_{1.95}$ Electrolyte-Based LT-SOFCs", In Meeting Abstracts", ***The Electrochemical Society,*** Vol. No. 16, (2012), 1976-1976.
11. Li, M., Hua, B., Luo, J. L., Jiang, S. P., Pu, J., Chi, B., Li, J., "Enhancing sulfur tolerance of Ni-based cermet anodes of solid oxide fuel cells by ytterbium-doped barium cerate infiltration", ***ACS Applied Materials & Interfaces***, Vol. 8, No. 16, (2016), 10293-10301.
12. Steele, B. C., Heinzel, A., "Materials for fuel-cell technologies", ***Nature***, Vol. 414, (2001), 345-352.
13. Litster, S., McLean, G., "PEM fuel cell electrodes", ***Journal of Power Sources***, Vol. 130, No. 1-2, (2004), 61-76.
14. Holton, O.T., Stevenson, J.W., "The role of platinum in proton exchange membrane fuel cells", ***Platinum Metals Review***, Vol. 57, No. 4, (2013), 259-271.
15. Chao, C.C., Motoyama, M., Prinz, F.B., "Nanostructured Platinum Catalysts by Atomic-Layer Deposition for Solid-Oxide Fuel Cells", ***Advanced Energy Materials***, Vol. 2, No. 6, (2012), 651-654.
16. O'Hayre, R., Cha, S.W., Colella, W., Prinz, F. B., "Fuel Cell Fundamentals", Hoboken, NJ: J. Wiley & Sons, (2009).
17. Hussain, A.M., Høgh, J.V., Zhang, W., Bonanos, N., "Efficient ceramic anodes infiltrated with binary and ternary electrocatalysts for SOFCs operating at low temperatures", ***Journal of Power Sources***, Vol. 216, (2012), 308-313.
18. Price, R., Cassidy, M., Schuler, J.A., Mai, A., Irvine, J.T., "Development and Testing of Impregnated $La_{0.20}Sr_{0.25}Ca_{0.45}TiO_3$ Anode Microstructures for Solid Oxide Fuel Cells", ***ECS Transactions***, Vol. 78, No. 1, (2017), 1385-1395.
19. Birss, V.I., Chang, M., Segal, J., "Platinum oxide film formation-reduction: an in-situ mass measurement study", ***Journal of Electroanalytical Chemistry***, Vol. 355, No. 1-2, (1993), 181-191.
20. Moulijn, J.A., Van Diepen, A.E., Kapteijn, F., "Catalyst deactivation: is it predictable?: What to do?", ***Applied Catalysis A: General***, Vol. 212, No. 1-2, (2001), 3-16.
21. Bernardi, F., Alves, M.C., Morais, J., "Monitoring of Pt nanoparticle formation by H2 reduction of PtO_2: an in situ dispersive x-ray absorption spectroscopy study", ***The Journal of Physical Chemistry C***, Vol. 114, No. 49, (2010), 21434-21438.
22. htpps://www.chemicalbook.com/ChemicalProductProperty_ EN_ CB1254558.htm.
23. htpps://www.periodni.com/ pt.html.
24. htpps://hypertextbook.com/facts/2004/OliviaTai.shtml.
25. Barin, I., Platzki, G., "Thermochemical data of pure substances", 3rd ed., VCH Verlagsgesellschaft mbH, Weinheim, New York, (1995).
26. Kleitz, M., Petitbon, F., "Optimized SOFC electrode microstructure", ***Solid State Ionics***, Vol. 92, No. 1-2, (1996), 65-74.